PHYSICAL REVIEW E **100**, 012201 (2019)

Sensitivity of chaotic behavior to low optical frequencies of a double-beam torsional actuator

F. Tajik,[1,4] M. Sedighi,[2] A. A. Masoudi,[1] H. Waalkens,[3] and G. Palasantzas[4,*]
[1]*Department of Physics, Alzahra University, Tehran 1993891167, Iran*
[2]*New Technologies Research Center (NTRC), Amirkabir University of Technology, Tehran 15875-4413, Iran*
[3]*Bernoulli Institute for Mathematics, Computer Science and Artificial Intelligence, University of Groningen, Nijenborgh 9, 9747 AG Groningen, Netherlands*
[4]*Zernike Institute for Advanced Materials, University of Groningen, Nijenborgh 4, 9747 AG Groningen, Netherlands*

(Received 22 February 2019; revised manuscript received 15 May 2019; published 1 July 2019)

We investigate here how the optical properties at low frequencies affect the actuation dynamics and emerging chaotic behavior in a double-beam torsion actuator at nanoscale separations (<200 nm), where the Casimir forces and torques play a major role. In fact, we take into account differences of the Casimir force due to alternative modeling of optical properties at low frequencies, where measurements are not feasible, via the Drude and plasma models, and repercussions by different material preparation conditions. For conservative autonomous actuation, bifurcation and phase portrait analysis indicate that both factors affect the stability of an actuating device in such a way that stronger Casimir forces and torques will favor increased unstable behavior. The latter will be enhanced by unbalanced application of electrostatic voltages in double-beam actuating systems. For the case of a time-periodic driving force, we use a Melnikov function and a phase plane analysis to study the emerging chaotic behavior with respect to the Drude and plasma modeling and material preparation conditions. We find indications that any factor that leads to stronger Casimir interactions will aid chaotic behavior and prevent long term prediction of the actuating dynamics. Moreover, in a double-beam actuator chaoticity will be amplified by the application of unbalanced electrostatic voltages. Therefore, the details of modeling of optical properties and the material preparations conditions must be carefully considered in the design of actuating devices at nanoscale because here Casimir forces are omnipresent and broadband type interactions.

DOI: 10.1103/PhysRevE.100.012201

I. INTRODUCTION

Nowadays advances in microfabrication techniques have pushed microelectromechanical systems (MEMS) to enter the submicron length scales, and simultaneously unravel the significant role of Casimir forces in nanoengineering [1–6]. Unlike electrostatic forces, which can be switched on and off by applying a potential, the Casimir force is always omnipresent and can set fundamental limitations on the design of micronanodevices [2,3,7,8]. This is because at separations less than 200 nm [9] the ratio of surface area to distance in MEMS components is large enough for the Casimir force to play a significant role, and pull components together leading to their permanent adhesion, which is a phenomenon known as stiction [1,2,10,11]. In fact, the Casimir force was predicted by Casimir [6] who proved that two perfectly conducting parallel plates attract each other due to perturbations of quantum vacuum fluctuations of the electromagnetic (EM) field. Later, Lifshitz and co-workers [12] considered the general case of dielectric plates by exploiting the fluctuation-dissipation theorem (FDT), which relates the dissipative properties of the plates (optical absorption by many dipoles) and the resulting EM fluctuations. In fact, the Lifshitz theory [12] predicts the attractive force between two parallel plates of arbitrary materials, and covers both the van der Waals (short range) and Casimir (long range) asymptotic regimes. The dependence of the Casimir force on material optical properties is an important outcome of the Lifshitz theory, and in principle, can be used to tailor the performance of actuating devices.

The normal Casimir force can also cause mechanical Casimir torques in torsional electrostatic actuators [13–17]. These devices have a wide range of applications such as, for example, torsional radio frequency (rf) switches, tunable torsional capacitors, torsional micromirrors, and high precision Casimir force measurements [1,2,4,10]. In fact, the torsional actuator is composed of two electrodes, one of which is fixed and the other is able to rotate around an axis. By applying a voltage between the electrodes, the moving electrode can rotate and, under conditions resulting in an imbalance between the Casimir and electrostatic forces, the rotating electrode can become unstable and collapse on the fixed one [18]. However, analyzing actuation dynamics by considering Casimir forces and torques requires proper calculation of these interactions taking properly into account the optical properties of the interacting materials in the low frequency regime from the infrared (IR) to the static limit ($\omega \to 0$) [19]. Indeed, Casimir force measurements have revealed deviations from predictions of dissipation models that are used to extrapolate at low optical frequencies where measurements of the optical response are not feasible [10]. For example, the Drude (D) model leads to finite absorption at frequencies $\omega > 0$ and singular absorption $\sim 1/\omega$ for $\omega \to 0$. On the other hand, the plasma (P) model, which can be thought of as having infinite absorption at the

---

[*] g.palasantzas@rug.nl

2470-0045/2019/100(1)/012201(13)

frequency $\omega = 0$ and zero anywhere else, allowed calculations of the Casimir force that described the measured force data more precisely at separations above 160 nm [10,11].

So far several investigations have been conducted to study the actuation dynamics of torsional actuators under the influence of Casimir and electrostatic forces for a wide range of material optical properties [8,20,21]. From these studies it has emerged that chaotic behavior is unavoidable during actuation dynamics, which leads to increased possibility for stiction and consequently limiting the long term prediction of devices to perform stable operation. However, the implications of Drude and plasma models on the chaotic motion of nanoscale devices have not been investigated in detail within the strong force and/or torque regime at short separations (<200 nm). Independent of the actual physical reason for this discrepancy—which has remained unresolved for more than 15 years in the Casimir field, e.g., a signature of either an inconsistency in the Lifshitz theory or a contribution of electrostatic surface potentials—this uncertainty is a fact that has to be properly assessed in actuation dynamics as it will be shown in the present work for the case of torsional oscillators. For this purpose we consider the torsional oscillators to be coated with gold (Au) but under different preparation conditions leading to variation of optical properties and static conductivity ratios $\omega_p{}^2/\,\omega_\tau$ [19], and we explored the sensitivity of chaotic behavior on the Drude and plasma models by also taking into account electrostatic forces.

II. OPTICAL PROPERTIES AND ACTUATION MODEL

The optical properties of the Au samples in this study were commercially characterized with ellipsometry [22] using VUV-VASE (0.5–9.34 eV) and IR-VASE (0.03–0.5 eV) ellipsometers with high spectral resolution. Subsequently, the real and imaginary parts of the frequency dependent dielectric function $\varepsilon(\omega)$ have been extracted and analyzed [19]. From the measured optical data, the dielectric functions at imaginary frequencies ξ, $\varepsilon(i\xi)$, being an essential quantity to calculate the Casimir force via the Lifshitz theory (see the Appendix), are shown in Fig. 1 for both the Drude and the plasma models. For this purpose, we have considered the two extreme cases of Au films with respect to the corresponding experimentally obtained plasma frequency ω_p for Au: (i) sample 1 with $\omega_p = 6.7$ eV and $\omega_\tau = 38.4$ meV, and (ii) sample 5 with $\omega_p = 8.37$ eV and $\omega_\tau = 37.1$ meV from [19]. The parameter ω_τ is the relaxation frequency of the Drude model (see the Appendix).

Furthermore, the inset of Fig. 1 illustrates the double-beam torsional actuator, where only the upper plate can rotate without any buckling deformation. It is assumed that both plates are coated with optically bulk Au (film thickness ⩾100 nm). The equation of torsional motion has the form

$$I_0\frac{d^2\theta}{dt^2} + \varepsilon I_0\frac{\omega}{Q}\frac{d\theta}{dt} = \tau_{\rm res} + \tau_{\rm elec} + \tau_{\rm Cas} + \varepsilon\,\tau_0\cos(\omega t), \quad (1)$$

with I_0 the moment of rotation inertia. For $\varepsilon = 0$, the torsional system performs corresponding autonomous conservative motion. The nonconservative forced motion with dissipation, which is driven by an externally applied electrostatic torque $\tau_0\cos(\omega t)$, corresponds to $\varepsilon = 1$.

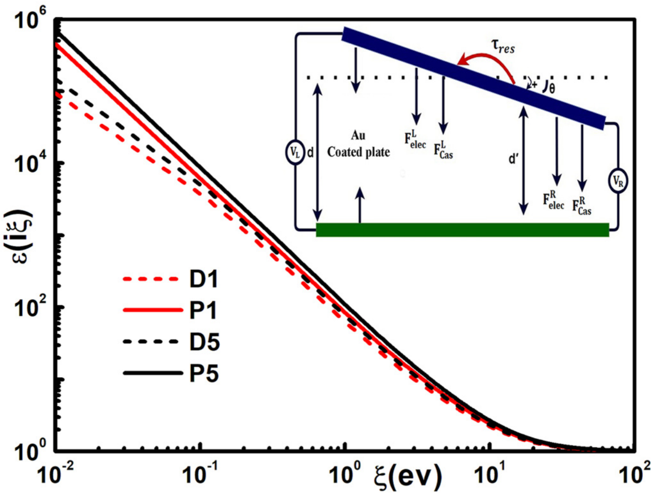

FIG. 1. Dielectric functions at imaginary frequencies $\varepsilon(i\xi)$ for Au for samples 1 and 5 of [19] using the Drude and plasma models. The samples 1 and 5 from [19] have conductivity ratios $\omega_p^2/\,\omega_\tau|_1 = 1169$ eV and $\omega_p^2/\,\omega_\tau|_5 = 1888.3$ eV, respectively. The inset shows the schematic of the double-beam torsional system.

The term $\tau_{\rm Cas}$ in Eq. (1) is the mechanical Casimir torque. The latter is given by [23]

$$\tau_{\rm Cas} = \int_0^{L_x} r\big[F^R_{\rm Cas}(d'_R) - F^L_{\rm Cas}(d'_L)\big]L_y\,dr, \quad (2)$$

where $F^{R,\,L}_{\rm Cas}(d'_{R,\,L})$ is the Casimir force that is calculated using Lifshitz theory (see the Appendix). L'_x $(=2L_x)$ and L_y are the length and width, respectively, of each plate (where we considered $L_x = L_y = 10\ \mu$m). $F^R_{\rm Cas}(d'_R)$ and $F^L_{\rm Cas}(d'_L)$ refer to the Casimir force on the right and left part of the rotating plate, with $d'_R = d - L_x\sin(\theta)$ and $d'_L = d + L_x\sin(\theta)$, respectively. The initial distance when the plates are parallel is assumed to be $d = 200$ nm, and the system temperature is fixed at room temperature, i.e., $T = 300$ K.

The total effective electrostatic torque $\tau_{\rm elec}$ acting on the rotating plate is given by $\tau_{\rm elec} = \tau^R_{\rm elec} - \tau^L_{\rm elec}$, where $\tau^R_{\rm elec}$ and $\tau^L_{\rm elec}$ are the electrostatic torques due to the applied potentials V^R_a and V^L_a at the right and left ends of the rotating plate, respectively. Upon substitution of the torques $\tau^{R,\,L}_{\rm elec}$ we obtain for the total electrostatic torque $\tau_{\rm elec}$ [16,17,23,24]

$$\tau_{\rm elec} = \frac{\varepsilon_0 L_y}{2\sin^2(\theta)}\left\{\left(V^R_a - V_c\right)^2\left[\ln\left(\frac{d'_R}{d}\right) + \frac{L_x\sin(\theta)}{d'_R}\right]\right.$$
$$\left. - \left(V^L_a - V_c\right)^2\left[\ln\left(\frac{d'_L}{d}\right) - \frac{L_x\,\sin(\theta)}{d'_L}\right]\right\}. \quad (3)$$

In Eq. (3) ε_0 is the permittivity of vacuum, and V_c is the contact potential difference between the interacting materials of the plates [25]. For simplicity, we will consider only the potential difference $V_{L,R} = V^{L,R}_a - V_c$ for the torque calculations. In any case, both the Casimir and electrostatic torques in Eq. (1) are counterbalanced by the restoring torque $\tau_{\rm res} = -k\theta$, with k the torsional spring constant at the support point of the rotating beam [26]. The term $I_0(\omega/Q)(d\theta/dt)$ corresponds to the intrinsic energy dissipation of the moving beam with Q the quality factor. The frequency ω is assumed to have a value

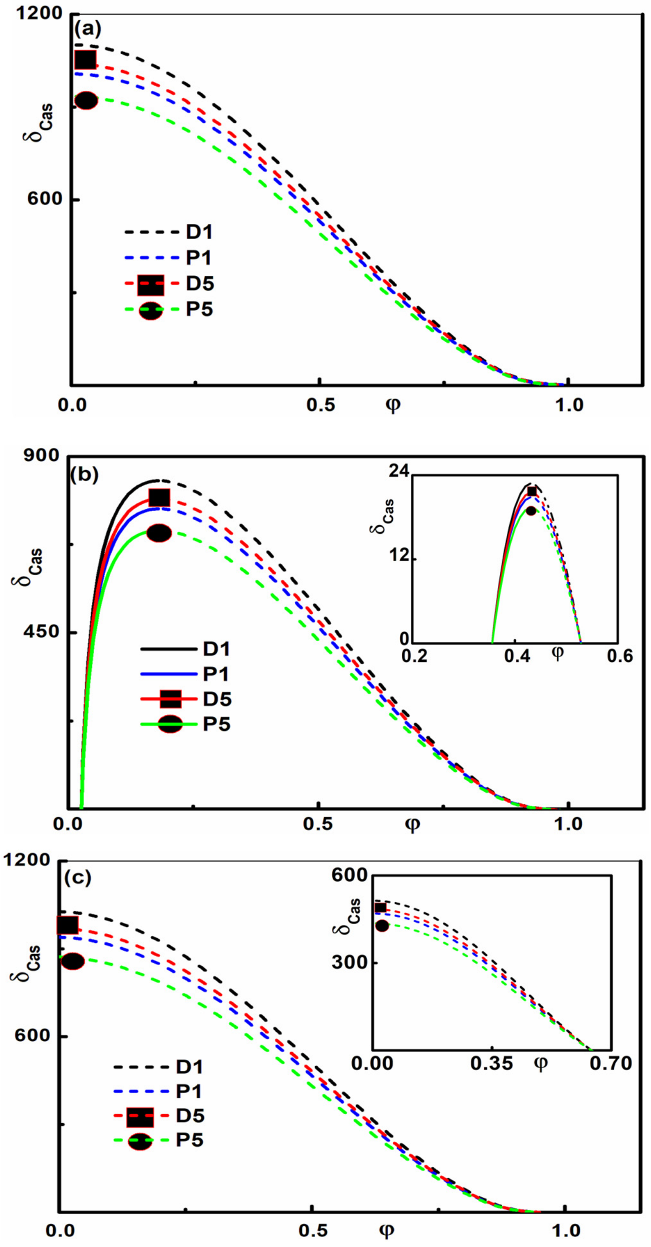

FIG. 2. Bifurcation diagrams $\delta_{\rm Cas}$ vs φ using the Drude and plasma models with (a) $\delta_v = 0$; (b) $\delta_v = 0.05$ and $p = 0$ (inset: $p = 0$ and $\delta_v = 0.5$); and (c) $\delta_v = 0.05$ and $p = 1$ (inset: $p = 1$ and $\delta_v = 0.5$). The solid and dashed lines represent the stable and unstable points, respectively.

that is typical for many resonators like AFM (atomic force microscopy) cantilevers, and MEMS [2,10,13,27,28]. Notably the type of motion we consider here applies to the case when the beam does not elastically deform since we assume large beam lengths (L_x) and small torsional angles at maximum separation ($\theta_0 = d/L_x = 0.02 \ll 1$).

Finally, in order to investigate the actuation dynamics the dimensionless bifurcation parameter $\delta_{\rm Cas} = \tau^M_{\rm Cas} / k\theta_0$ is introduced, which represents the ratio of the maximal Casimir torque $\tau^M_{\rm Cas} = \tau_{\rm Cas}(\theta = \theta_0)$ (for the different Au samples and the corresponding Drude or plasma model for the optical properties) to the maximum restoring torque $k\theta_0$. The parameter $\delta_{\rm Cas}$ will determine when there is a stable periodic solution for the torsional system that corresponds to sufficient restoring torque that prevents jump to contact and consequently stiction of the moving plate [29,30]. Equation (1) can be rewritten in a normalized form in terms of $\delta_{\rm Cas}$, $\varphi = \theta/\theta_0$, and the bifurcation parameter of the electrostatic force $\delta_v = (\varepsilon_0 V^2 L_y L_x^3)/(2kd^3)$ [31], as follows:

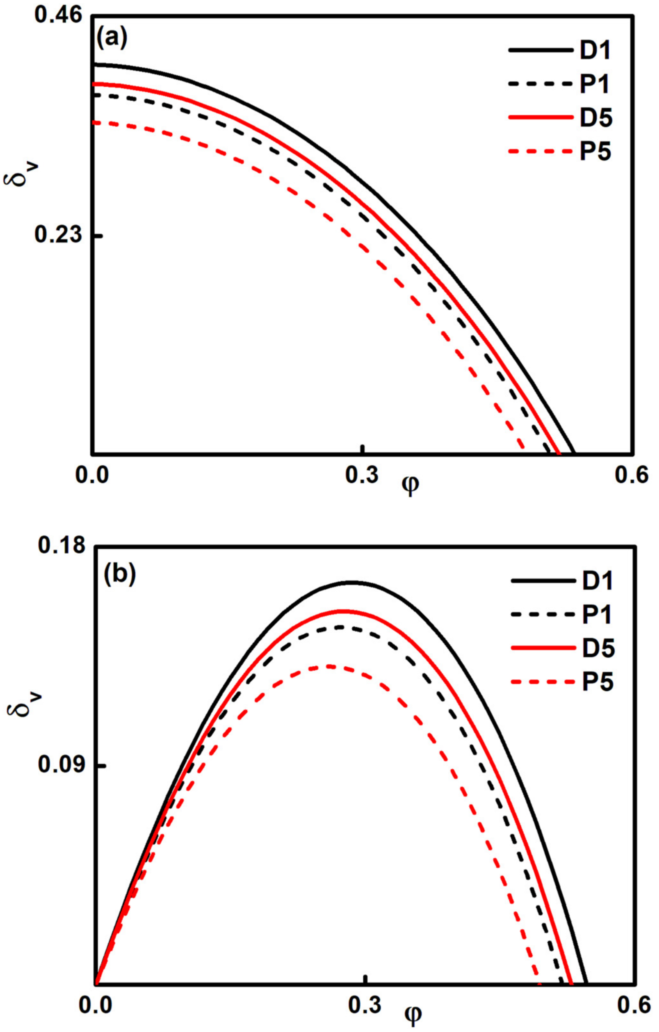

FIG. 3. Bifurcation diagrams δ_v vs φ using the Drude and plasma models, $\delta_{\rm Cas} = 500$, and for all studied samples: (a) $p = 1$, and (b) $p = 0$.

$$\begin{aligned}
&\frac{d^2\varphi}{dT^2} + \varepsilon\frac{1}{Q}\frac{d\varphi}{dT}\\
&\quad = -\varphi + \delta_v\frac{1}{\varphi^2}\left[\ln(1-\varphi) + \frac{\varphi}{1-\varphi}\right.\\
&\qquad \left. - p^2\left[\ln(1+\varphi) - \frac{\varphi}{1+\varphi}\right]\right]\\
&\qquad + \delta_{\rm Cas}\left[\frac{\tau_{\rm Cas}}{\tau^M_{\rm Cas}}\right] + \varepsilon\frac{\tau_0}{\tau^{\rm MAX}_{\rm res}}\cos\left(\frac{\omega}{\omega_0}T\right),
\end{aligned} \tag{4}$$

where $T = \omega_0 t$, $I = I_0/k$, and $p = V_L/V_R$ is the voltage ratio between the left and right sides of the beam.

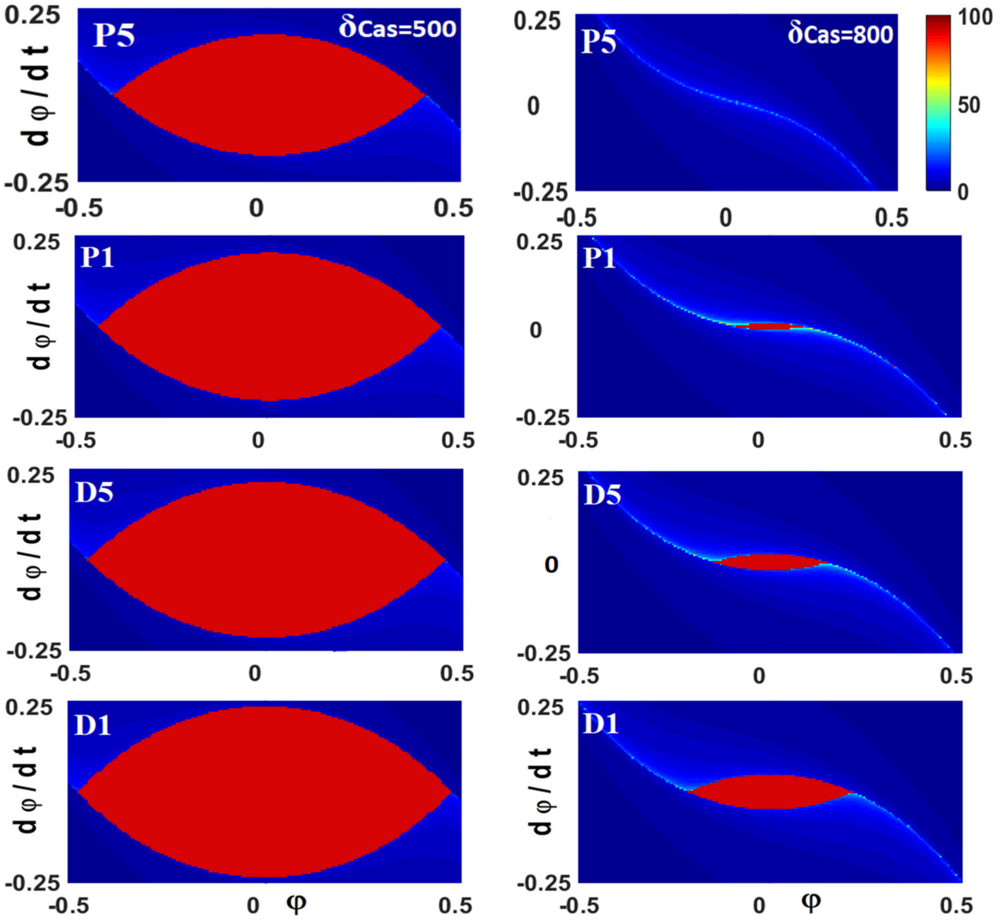

FIG. 4. Contour plot of the transient times to stiction in the phase plane $d\varphi/dt$ vs φ for $\delta_{\rm Cas}=500$ (left column) and $\delta_{\rm Cas}=800$ (right column), $\delta_v=0$, and initial conditions inside and outside of the heteroclinic orbit. The results with respect to the Drude and plasma models are shown in the left and right panels, respectively, for both samples 1 and 5.

III. CONSERVATIVE ACTUATION ($\varepsilon = 0$)

We will start our analysis with the conservative system, where the equilibrium points are obtained by the condition $\tau_{\rm total}=\tau_{\rm res}+\tau_{\rm elec}+\tau_{\rm Cas}=0$. As a result we obtain from Eq. (4) the equilibrium condition

$$-\varphi+\delta_v\frac{1}{\varphi^2}\left\{\ln(1-\varphi)+\frac{\varphi}{1-\varphi}-p^2\left[\ln(1+\varphi)-\frac{\varphi}{1+\varphi}\right]\right\}+\delta_{\rm Cas}\left[\frac{\tau_{\rm Cas}}{\tau^M_{\rm Cas}}\right]=0. \qquad (5)$$

Figure 2 depicts $\delta_{\rm Cas}$ vs φ for the two Au samples by taking into account the plasma and Drude models for both equal or $p=1$ ($V_R=V_L$), and unequal or $p\neq 1$ ($V_R\neq V_L$), electrostatic potentials. The strong effect of the applied electrostatic potential on the stability of the double beam has already been shown in [20]. In fact, when the electrostatic torque has equal magnitude at both ends of the beam ($V=0$ or $V_R=V_L$), the equilibrium points in the bifurcation diagram (except for $\varphi=0$) are always unstable. In addition, when the electrostatic potential is applied on one end of the beam ($p=0$ and $V_R>0$) the system shows the same bifurcation diagrams as for a single torsional beam. In Fig. 2(b) the solid lines indicate the stable regions, where the restoring torque $\tau_{\rm res}$ is strong enough to support stable periodic motion (since $\delta_{\rm Cas}\sim 1/k$), while the dashed lines indicate regions where the device becomes unstable and undergoes stiction for motion close to the fixed plate.

The presence of two equilibrium points occurs if $\delta_{\rm Cas}<\delta^{\rm MAX}_{\rm Cas}$, where the equilibrium point closer to $\varphi=0$ (solid line) is a stable center point, and the other one which is closer to $\varphi=1$ (dashed line) is an unstable saddle point. Therefore, according to Figs. 2(a) and 2(c) (electrostatically balanced cases) when $\delta_{\rm Cas}<\delta^{\rm MAX}_{\rm Cas}$ the bifurcation curves show solely one unstable equilibrium point for the system, and a permanently stable equilibrium point at $\varphi=0$. The unstable equilibria satisfy the additional condition $d\tau_{\rm total}/d\varphi=0$, which yields

$$-1+\delta_v\left[\frac{2\varphi-3}{\varphi^2(1-\varphi)^2}+\frac{2\ln(1-\varphi)}{\varphi^3}-P^2\left[\frac{2\varphi+3}{\varphi^2(1+\varphi)^2}+\frac{2\ln(1-\varphi)}{\varphi^3}\right]\right]+\delta_{\rm Cas}\frac{1}{\tau^m_{\rm Cas}}\left(\frac{d\tau_{\rm Cas}}{d\varphi}\right)=0. \qquad (6)$$

By increasing $\delta_{\rm Cas}$ or equivalently weakening the restoring torque ($\delta_{\rm Cas}\sim 1/k$), the distance between the stable and

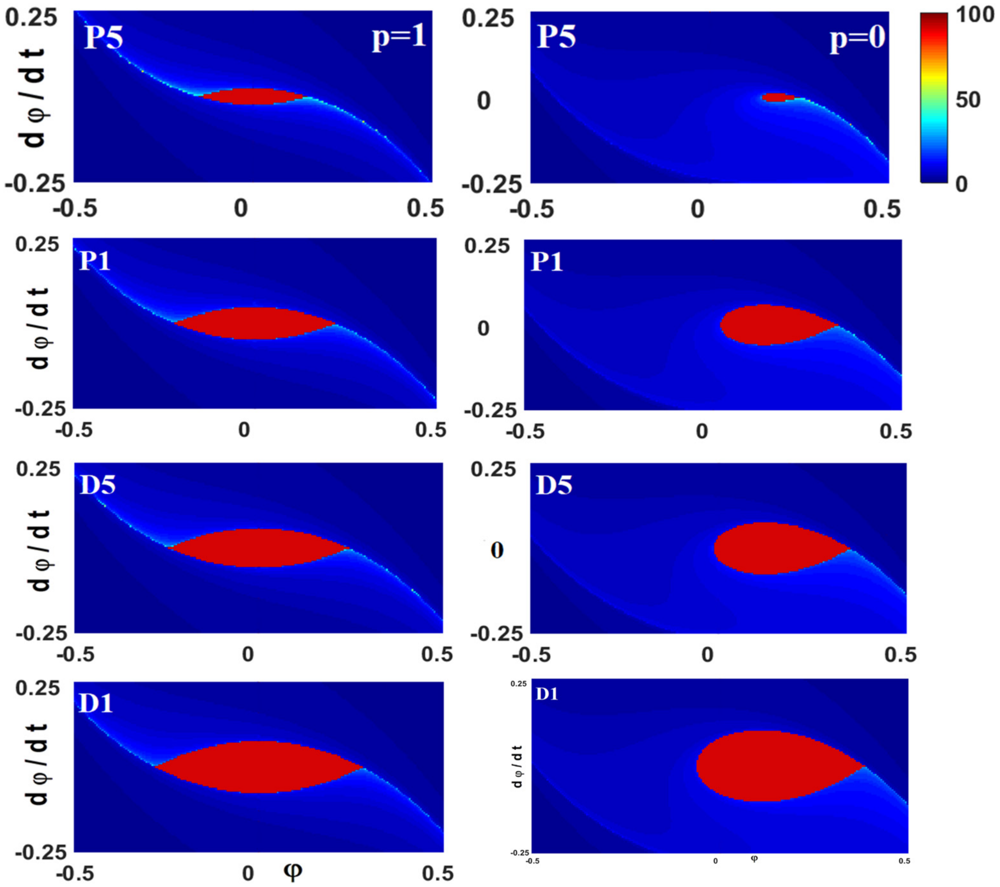

FIG. 5. Contour plot of the transient times to stiction in the phase plane $d\varphi/dt$ vs φ for samples 1 and 5 with $p = 1$ (left column, $\delta_{\mathrm{Cas}} = 500$ and $\delta_v = 0.22$), $p = 0$ (right column, $\delta_{\mathrm{Cas}} = 500$ and $\delta_v = 0.08$), as well as initial conditions inside and outside of the heteroclinic or homoclinic orbit. The results for the Drude and plasma models are shown in the left and right panels, respectively.

unstable points decreases until the maximum saddle point $\delta_{\mathrm{Cas}}^{\mathrm{MAX}}$ is reached that satisfies both Eqs. (5) and (6).

From Fig. 2 it is evident that for the more conductive sample, or equivalently higher value for ω_p^2/ω_τ, applying the plasma model leads to unstable motion and subsequently stiction, while there are still two equilibrium points if the Drude model is used. In fact, with decreasing restoring torque, the bifurcation diagrams confirm that the plasma model predicts more likely unstable motion and stiction, while the weaker force for the Drude model could lead to stable motion. From the insets in Figs. 2(a) and 2(c) one can conclude that increasing the applied voltage leads to a decrement of $\delta_{\mathrm{Cas}}^{\mathrm{MAX}}$ for both the balanced and unbalanced cases, independent of the plasma or Drude model for the low frequency regime. Moreover, Fig. 3 illustrates that the electrostatic bifurcation parameter δ_v shows not only sensitive dependence on the conductivity of the Au samples but also on the model that is used for the calculation of the optical properties at low frequencies. In addition, the range of bifurcation parameters for stable periodic motion ($0 < \delta_{\mathrm{Cas}} < \delta_{\mathrm{Cas}}^{\mathrm{MAX}}$ and $\delta_v \geqslant 0$) is decreased when at low frequencies the plasma model is considered instead of the Drude model. Notably, for $\delta_{\mathrm{Cas}} > \delta_{\mathrm{Cas}}^{\mathrm{MAX}}$ the torsional device is unstable even in the absence of electrostatic torques ($\delta_v = 0$).

Furthermore, the dependence of the actuation dynamics on sample preparation methods and the details of modeling of the low optical frequency regime are also explored by means of a phase plane analysis. The results indicate strong dependency on both factors for the homoclinic and heteroclinic orbits between the saddle points, and the area of stable motion they enclose which consists of closed orbits around the center point. Indeed, Fig. 4 shows the dynamical behavior of torsional MEMS in the absence of electrostatic forces ($V = 0$). The size of the stable area is strongly dependent on the optical properties at low frequencies, and this dependency becomes more significant by increasing the magnitude of the Casimir bifurcation parameter. The phase plane in the right column of Fig. 4 clarifies that for a system with stronger Casimir attraction (sample 5, $\omega_p^2/\omega_\tau = 1893.4\,\mathrm{eV}$) the details of the modeling of the low optical frequency regime as $\omega \rightarrow 0$ can predict either stable motion (Drude model) or stiction dynamics (plasma model) at nanoscale separations <200 nm, where the surface interactions are strong enough to pull components together. However, such a discrepancy is reduced for the less conductive system (sample 1, $\omega_p^2/\omega_\tau = 1169\,\mathrm{eV}$). Finally, Fig. 5 shows how the size of the area enclosed by the heteroclinic and homoclinic orbits decreases with increasing conductivity ($\sim\omega_p^2/\omega_\tau$) of the interacting materials. For any initial conditions outside the heteroclinic and homoclinic orbits, the moving beam will perform unstable motion and will quickly collapse on the fixed plate with the homoclinic orbits being more susceptible to the modeling details of the low optical frequency regime.

IV. NONCONSERVATIVE ACTUATION ($\varepsilon = 1$)

Here we investigate the existence of chaotic behavior of the torsional system undergoing forced oscillations driven by an externally applied torque $\tau_o \cos(\omega t)$. In fact, chaotic behavior can occur if the separatrix (heteroclininc or homoclinic orbit) of the conservative system splits. This dynamical behavior can be studied by the so-called Melnikov function and a phase plane analysis [15,32]. The Melnikov functions for the torsional system are given by [8,33–35]

$$M^{\rm het}(T_0) = \frac{1}{Q}\int_{-\infty}^{+\infty}\left[\frac{d\varphi^C_{\rm het}(T)}{dT}\right]^2 dT + \frac{\tau_0}{\tau^{\rm MAX}_{\rm res}}\int_{-\infty}^{+\infty}\frac{d\varphi^C_{\rm het}(T)}{dT} \times \cos\left[\frac{\omega}{\omega_0}(T - T_0)\right]dT, \tag{7}$$

and

$$M^{\rm hom}(T_0) = \frac{1}{Q}\int_{-\infty}^{+\infty}\left[\frac{d\varphi^C_{\rm hom}(T)}{dT}\right]^2 dT + \frac{\tau_0}{\tau^{\rm MAX}_{\rm res}}\int_{-\infty}^{+\infty}\frac{d\varphi^C_{\rm hom}(T)}{dT}\cos\left[\frac{\omega}{\omega_0}(T + T_0)\right]dT. \tag{8}$$

Moreover, we define the heteroclinic and homoclinic solution of the conservative system as $\varphi^C_{\rm het}(T)$ and $\varphi^C_{\rm hom}(T)$, respectively. The separatrix splits, if the Melnikov function has simple zeros, so that $M^{\rm het/hom}(T_0) = 0$ and $(M^{\rm het/hom})'(T_0) \neq 0$. If $M^{\rm het/hom}(T_0)$ has no zeros, then the motion will not be chaotic. The conditions of nonsimple zeros, namely, $M^{\rm het/hom}(T_0) = 0$ and $(M^{\rm het/hom})'(T_0) = 0$, give the threshold condition for chaotic motion [33,34]. If we define

$$\mu^c_{\rm het/\,hom} = \int_{-\infty}^{+\infty}\left[\frac{d\varphi^C_{\rm het/\,hom}(T)}{dT}\right]^2 dT, \quad \text{and}$$

$$\beta_{\rm het/\,hom}(\omega) = \left|H\left({\rm Re}\left\{F\left[\frac{d\varphi^C_{\rm het/\,hom}(T)}{dT}\right]\right\}\right)\right|, \tag{9}$$

then the threshold condition for chaotic motion $\alpha = \beta_{\rm het/hom}(\omega)/\mu^c_{\rm het/hom}$ with $\alpha = (1/Q)(\tau_0\,/\tau^{\rm MAX}_{\rm res})^{-1} = \gamma\omega_{0\ \theta_0}/\tau_0$ obtains the form

$$\alpha = \frac{\gamma\omega_{0\ \theta_0}}{\tau_0} = \left|H\left({\rm Re}\left\{F\left[\frac{d\varphi^C_{\rm het/\,hom}(T)}{dT}\right]\right\}\right)\right| \Big/ \times \int_{-\infty}^{+\infty}\left[\frac{d\varphi^C_{\rm het/\,hom}(T)}{dT}\right]^2 dT. \tag{10}$$

with $\gamma = {\rm I}\omega_o/Q$, and $H(\cdots)$ denoting the Hilbert transform [20,33].

Figures 6–8 show the threshold curves $\alpha = \gamma\omega_{0\theta_0}/\tau_0$ vs the driving frequency ω/ω_o. It is evident that for large values of α (above the curve) the dissipation dominates the energy gained by the external driving torque leading to regular motion that asymptotically approaches the stable periodic orbit of the conservative system. However, for parameter values below the curve, the transversal intersections of the stable and unstable manifolds could cause chaotic motion and subsequent stiction. For systems with the higher conductivity and therefore stronger Casimir torques, chaotic motion is more likely to occur as it is manifested by the larger area below the threshold curves. More specifically, Figs. 6(a) and 6(b) show that the threshold condition evolves for samples 1 and 5 in the absence of any applied voltage. The area below the curve exhibits strong dependence on the sample preparation, and the model that is used for the extrapolation at low optical frequencies. In fact, the Drude model will decrease the possibility of chaotic behavior in comparison to the plasma model. In addition, Figs. 7 and 8 show the threshold condition in the presence of electrostatic forces for balanced and unbalanced situations, respectively. For the unbalanced case, the possibility of chaotic motion by application of voltage, which can be interpreted by the change of the area below the threshold curve, is higher in comparison to the balanced case.

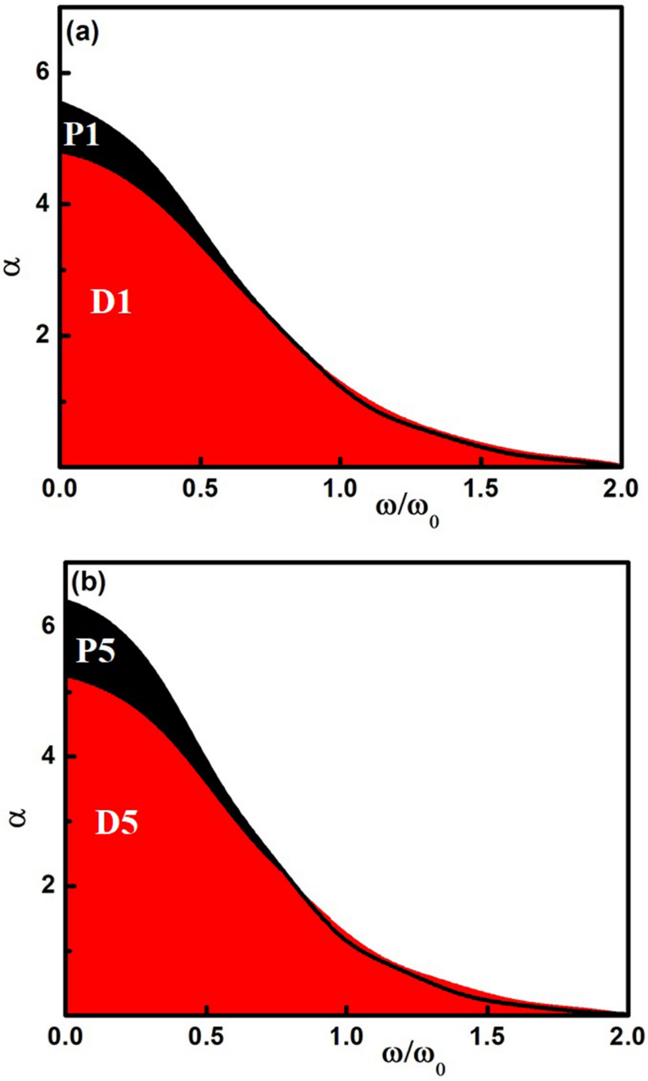

FIG. 6. Threshold curve α ($=\gamma\omega_{0\theta_0}/\tau_0$) vs. driving frequency ω/ω_o (with ω_o the natural frequency of the system). The area bellow the curve corresponds to parameters that could lead to chaotic motion with $\delta_{\rm Cas} = 500$ and $\delta_v = 0$ for both the Drude and plasma models: (a) sample 1, and (b) sample 5.

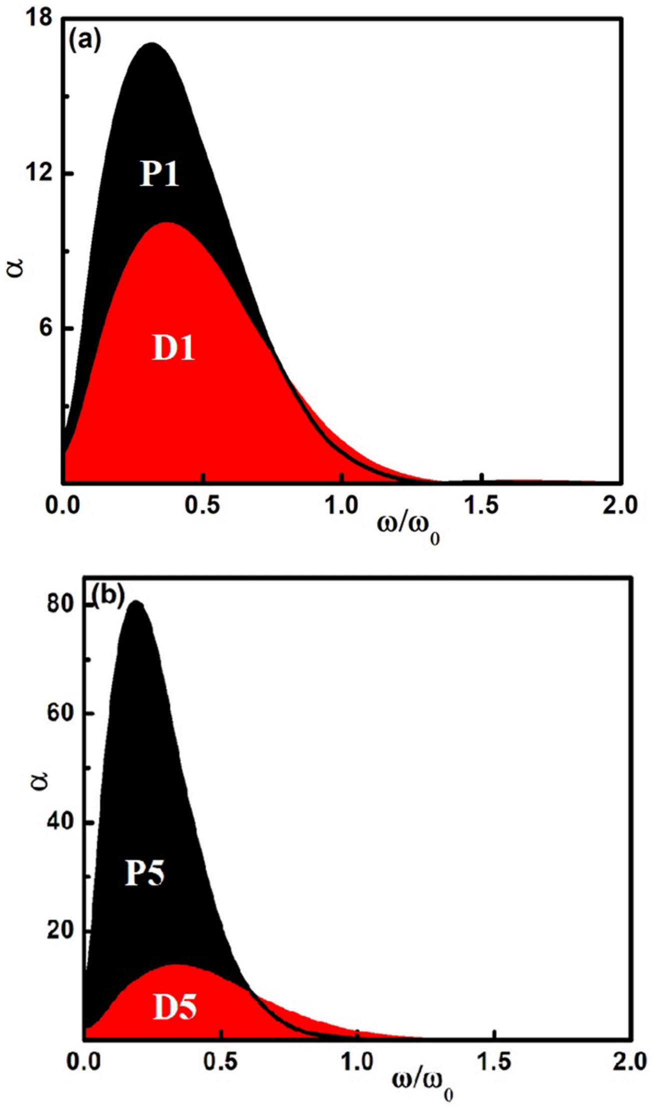

FIG. 7. Threshold curve α $(=\gamma\omega_{0\theta_0}/\tau_0)$ vs driving frequency ω/ω_o (with ω_o the natural frequency of the system). The area below the curve corresponds to parameters that could lead to chaotic motion with $\delta_{\rm Cas} = 500$, $\delta_v = 0.08$, and $p = 0$ (unbalanced case) for both the Drude and plasma models: (a) sample 1, and (b) sample 5.

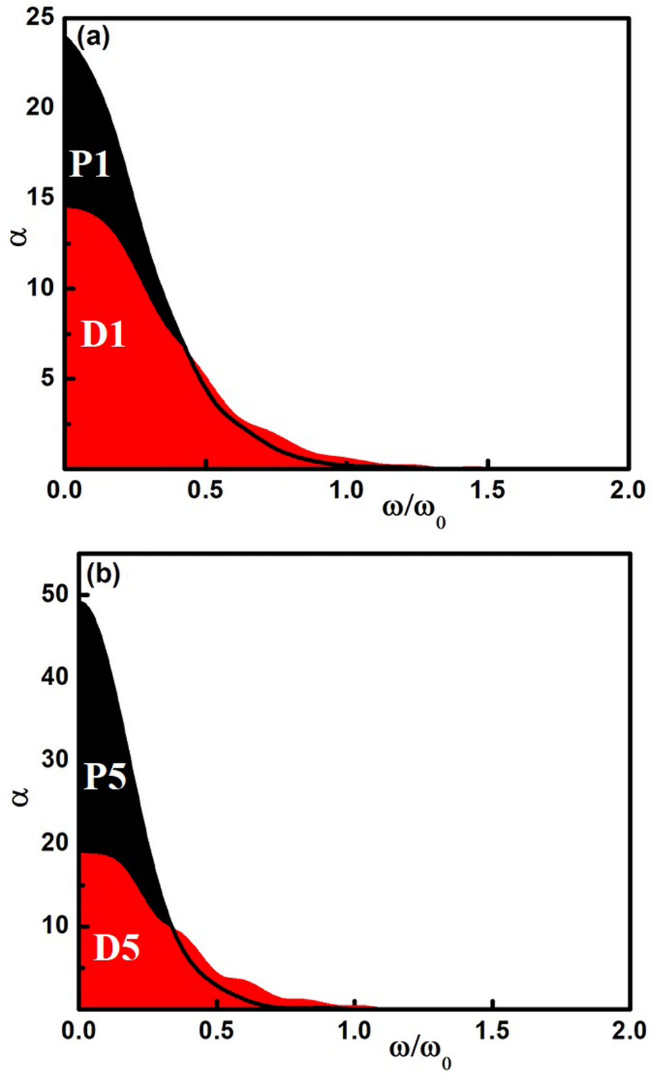

FIG. 8. Threshold curve α $(=\gamma\omega_{0\theta_0}/\tau_0)$ vs driving frequency ω/ω_o (with ω_o the natural frequency of the system). The area below the curve corresponds to parameters that can lead to chaotic motion with $\delta_{\rm Cas} = 500$, $\delta_v = 0.22$, and $p = 1$ (balanced case) for both the Drude and plasma models: (a) sample 1, (b) sample 5.

Furthermore, a phase plane analysis is shown in Figs. 9–12 to elucidate the effect of chaotic behavior. For all the calculations we used 150×150 initial conditions $(\varphi,\ d\varphi/dt)$, and the red region indicates the initial condition for which the torsional device still performs stable motion after 100 oscillations. Figure 9 illustrates the chaotic behavior for balanced, $p = 1$ (left column), and unbalanced, $p = 0$ (right column), torsional systems. From these plots it is evident how the optical properties in the low frequency regime and different samples can profoundly change the dynamical behavior of actuating devices. Indeed, the *red (elliptical shape) central area* which corresponds to stable actuation becomes smaller if we use the plasma model, and in addition this effect becomes even more significant with increasing sample conductivity (e.g., sample 5). Therefore, the phase plane analysis shows that increasing sample conductivity (depending on preparation conditions) enhances the occurrence of chaotic motion [32] and as a result reduces the ability to predict the long term behavior of the actuating system.

Figures 10 and 11 indicate in more detail the effect of applied voltages for both samples, and considering both the Drude and plasma models. By imposing the same level of applied voltage, the stability of an electrostatically balanced double beam $(p = 1)$ is significantly enhanced in comparison to the unbalanced case $(p = 0)$ in agreement also with the Melnikov analysis. In Fig. 12 we also illustrate the sensitive dependence of the emergent chaotic motion on the modeling of the low frequency regime for the highest conductivity sample. Indeed, changing from the Drude to the plasma model, which has a larger value for the bifurcation parameter $\delta_{\rm Cas}$, the whole *red (elliptical shape) central area* that corresponds to stable motion totally vanishes with chaotic motion dominating the torsional system. If the value of (first column) is reduced,

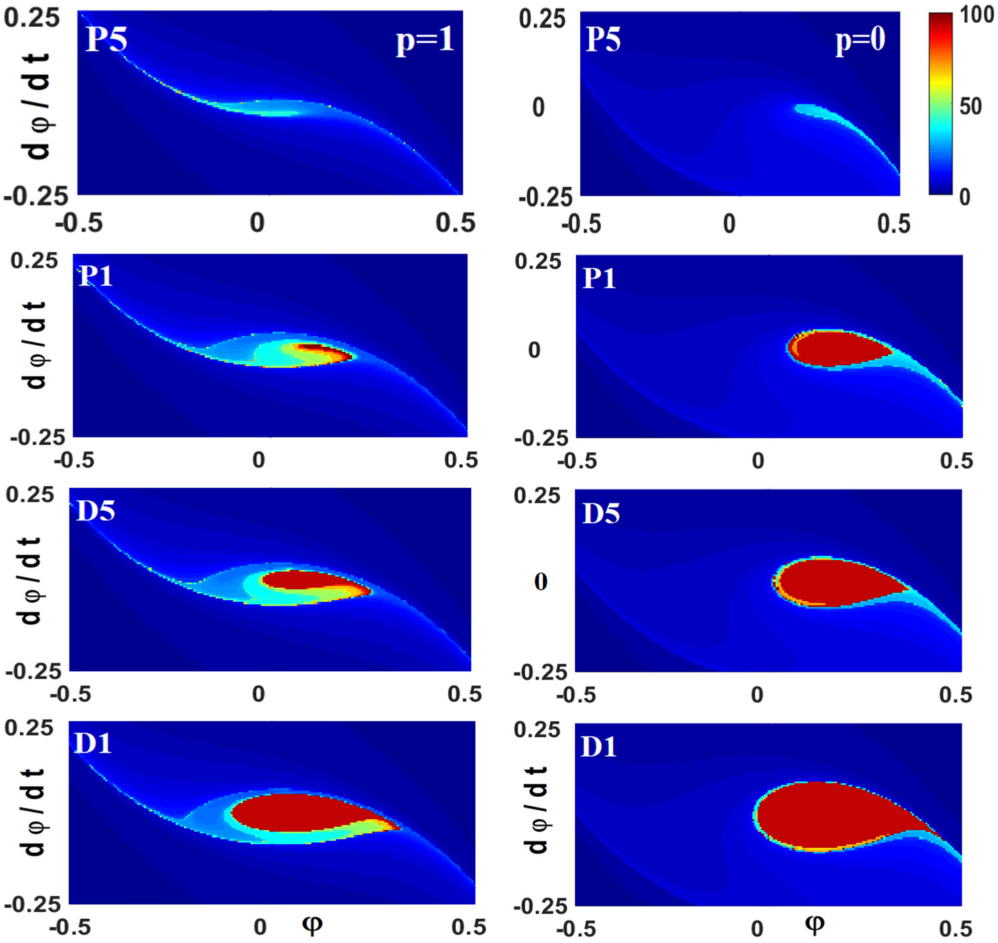

FIG. 9. Contour plot of the transient times to stiction in the phase plane $d\varphi/dt$ vs φ for the nonconservative system with $\alpha = 0.5$ and $\omega/\omega_o = 0.2$: $p = 1$ (balanced case, left column for $\delta_{\mathrm{Cas}} = 500$ and $\delta_v = 0.22$), and $p = 0$ (unbalanced case, right column for $\delta_{\mathrm{Cas}} = 500$ and $\delta_v = 0.08$) for samples 1 and 5 with plasma model (right column) and Drude model (left column). *The red (light gray) elliptical shape central area corresponds to stable actuation.*

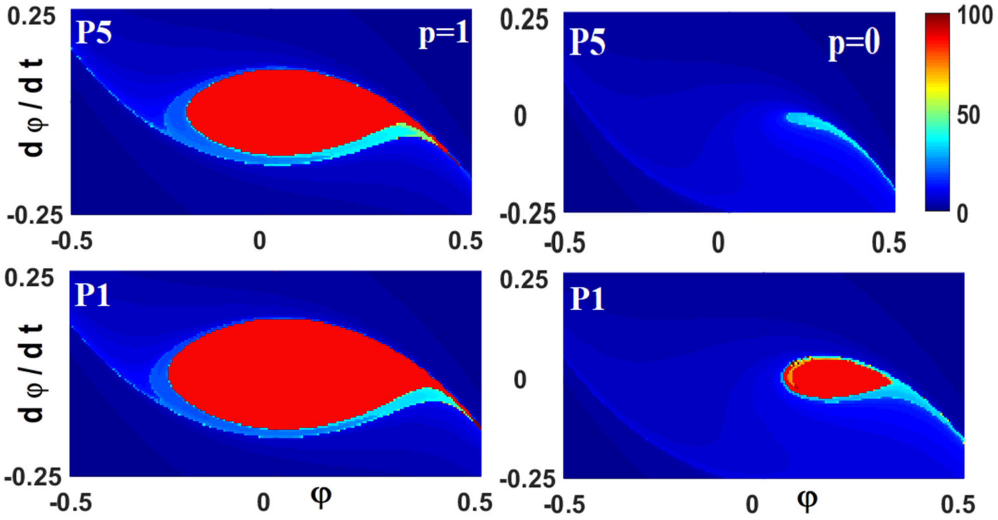

FIG. 10. Contour plot of the transient times to stiction in the phase plane $d\varphi/dt$ vs φ for the nonconservative system with $\alpha = 0.5$, $\omega/\omega_o = 0.2$, $\delta_{\mathrm{Cas}} = 500$, $\delta_v = 0.08$, and considering the plasma model for sample 1 and 5: $p = 0$ (unbalanced case, right column), and $p = 1$ (balanced case, left column).

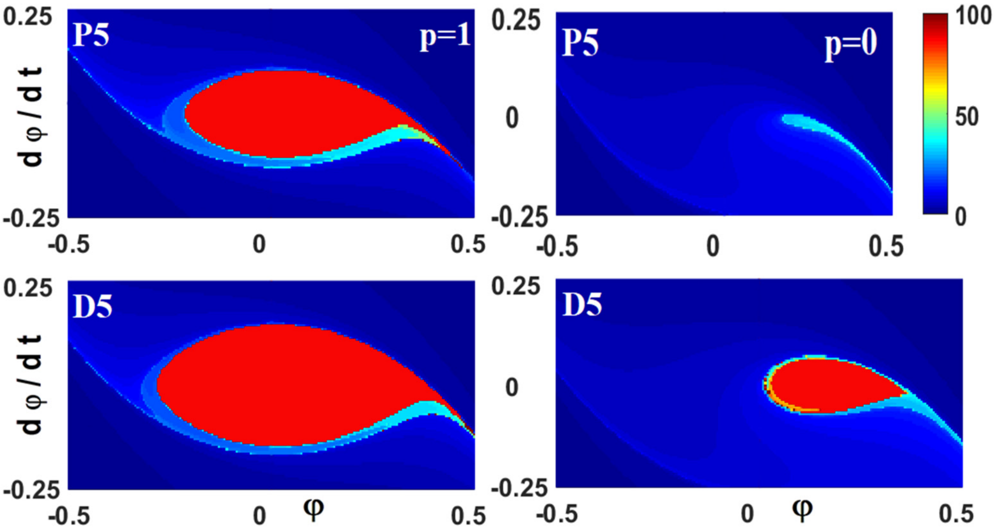

FIG. 11. Contour plot of the transient times to stiction in the phase plane $d\varphi/dt$ vs φ for the nonconservative system with $\alpha = 0.5$, $\omega/\omega_o = 0.2$, $\delta_{\text{Cas}} = 500$, $\delta_v = 0.08$ for sample 5 with respect to Drude and plasma models: $p = 0$ in right panel (unbalanced case), and $p = 1$ in left panel (balanced case).

then by changing from Drude to plasma models some part of the stable area will be preserved. The change of stable area as the number of oscillations N evolves, for both the Drude and plasma models, is shown in the phase planes of Figs. 13 and 14 for electrostatically balanced and unbalanced cases. Figure 15 shows quantitatively the change of the magnitude of the stable area from Figs. 13 and 14.

V. CONCLUSIONS

In conclusion, we investigated here how the optical properties at low frequencies affect the actuation dynamics and emerging chaotic behavior in a double-beam torsion actuator at nanoscale separations (<200 nm), where the Casimir forces and torques play a major role. Several MEMS devices that have been used for Casimir measurements were operated at relatively large separations (160–200 nm or more [2,10,28]) to avoid stiction instabilities. For our analysis, we took into account differences in modeling at low optical frequencies, where measured optical data are not available, and changes that occur due to different preparation conditions for the same material. Our focus is on the optical models on the Drude and plasma models that have been used in the literature to model low optical frequencies, but still their use remains an open problem in Casimir physics. For conservative autonomous actuation, bifurcation and phase plane analysis indicate that the details of the modeling of the low optical frequency regime can strongly affect the stability of an actuating device. In fact, higher Casimir forces and torques, due to higher material conductivity and optical models in use, will favor unstable behavior that will be enhanced by unbalanced application of voltages for double-beam actuating systems.

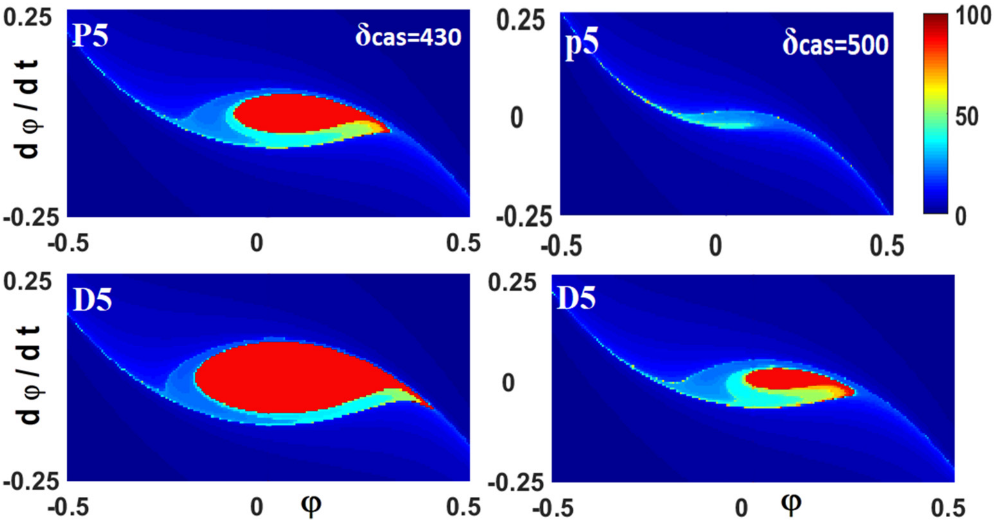

FIG. 12. Contour plot of the transient times to stiction in the phase plane $d\varphi/dt$ vs φ for the nonconservative system with $\alpha = 0.5$, $\omega/\omega_o = 0.2$, $\delta_v = 0.22$, sample 5, and $p = 1$ (balanced situation): $\delta_{\text{Cas}} = 500$ (right panel), and $\delta_{\text{Cas}} = 430$ (left panel). *The red (light gray) elliptical shape central area corresponds to stable actuation.*

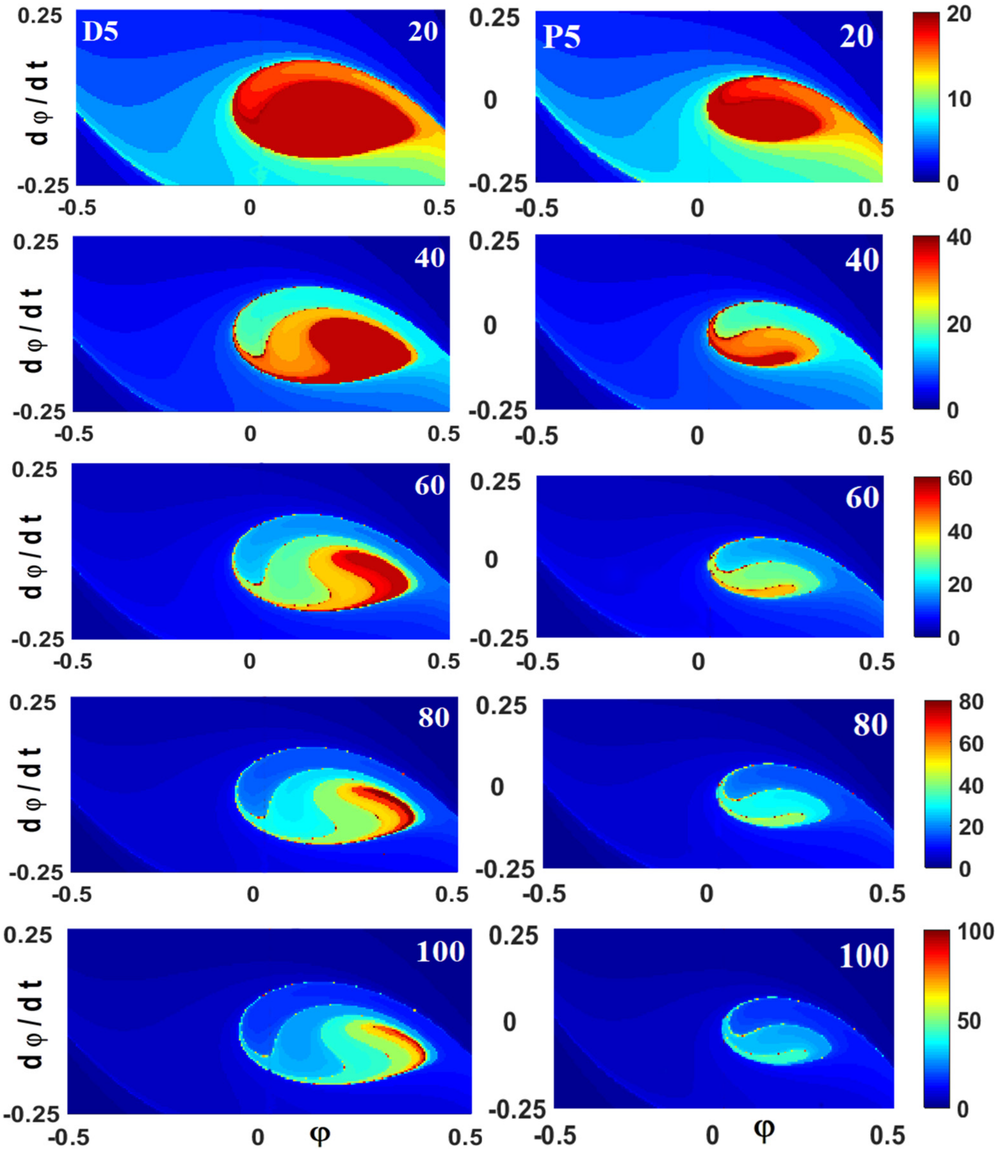

FIG. 13. Contour plot of the transient times to stiction in the phase plane $d\varphi/dt$ vs φ for sample 5 of the nonconservative system with $\alpha = 0.02$, $\omega/\omega_o = 0.5$, $p = 0$ (unbalanced case), $\delta_{\rm Cas} = 430$, and $\delta_v = 0.09$ for different oscillations cycles as indicated. Plasma model: right column, and Drude model: left column.

Furthermore, for nonconservative dynamics in nonlinear systems, we used the Melnikov and phase plane analysis to study the emerging chaotic behavior with respect to the Drude and plasma modeling and material preparation conditions indicating that any factor that leads to stronger Casimir interactions (which is the case for the plasma model) will aid chaotic behavior and stiction, as well as prevent long term prediction of the actuating dynamics. Moreover, in a double-beam actuator chaoticity is amplified by the application of unbalanced electrostatic voltages. Therefore, the details of modeling of optical properties at low optical frequencies via the Drude or the plasma models, and the material preparation conditions, must be carefully considered for reliable predictions of actuation dynamics, for any type of dynamical system when interacting surfaces come in close proximity, because the Casimir forces are omnipresent and broadband type interactions. As a result our investigations could aid those who work on solving the Drude-plasma model uncertainty by possible actuation experiments, since our analysis shows the strong impact of the low optical frequency modeling on actuation dynamics.

ACKNOWLEDGMENTS

G.P. acknowledges support from the Zernike Institute of Advanced Materials, University of Groningen. M.S. acknowledges support from the Amirkabir University of Technology. F.T. and A.A.M. acknowledge support from the Department of Physics at Alzahra University. A.A.M. acknowledges support from Iran National Science Foundation (INSF) under Grant No. 97002131. We would also like to acknowledge useful discussions with M. Khorrami.

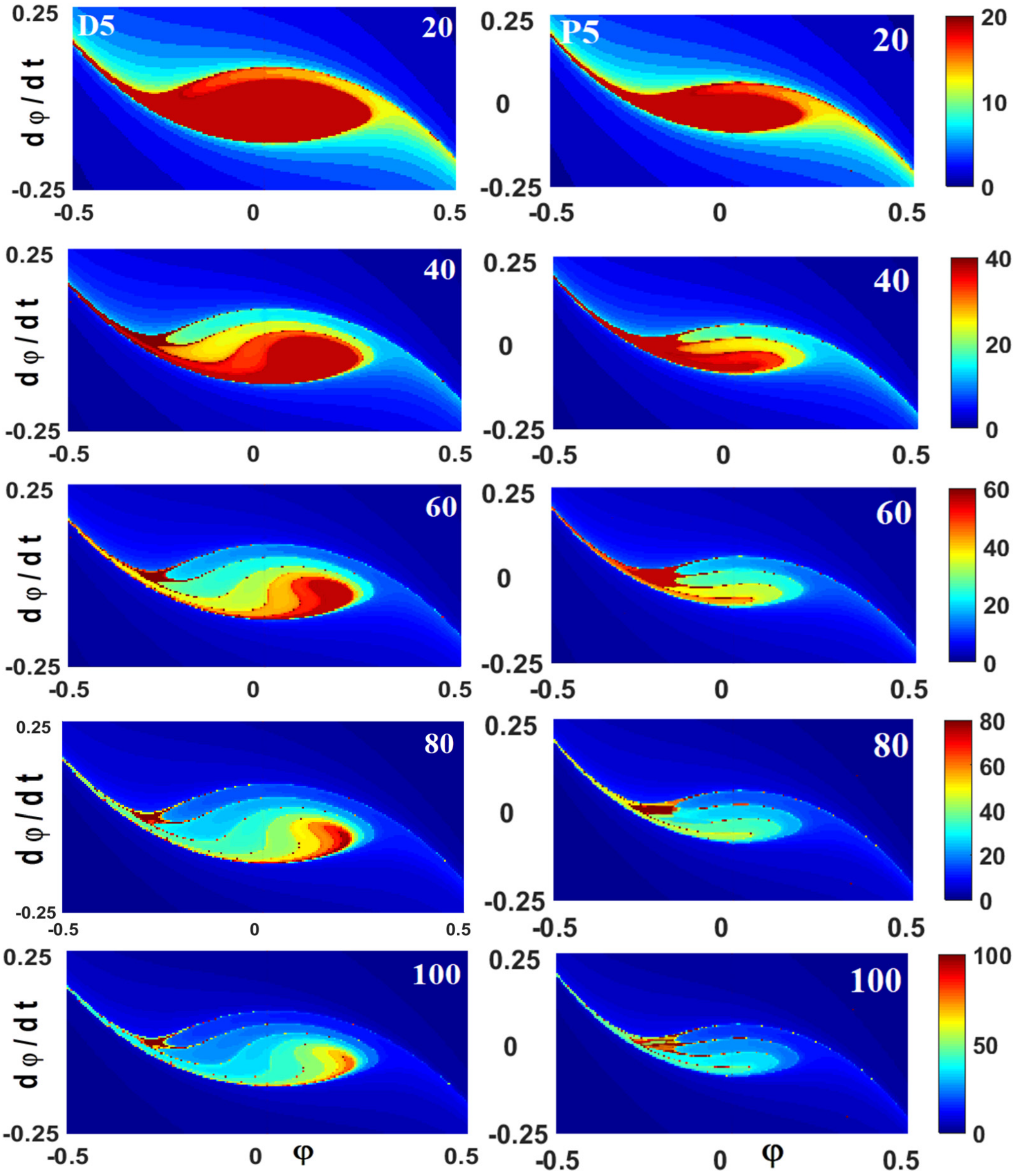

FIG. 14. Contour plot of the transient times to stiction in the phase plane $d\varphi/dt$ vs φ for sample 5 of the nonconservative system with $\alpha = 0.02$, $\omega/\omega_o = 0.35$, $\delta_{\mathrm{Cas}} = 430$, and $\delta_v = 0.22$ for different oscillation cycles. Plasma model: right column, and Drude model left column.

APPENDIX: LIFSHITZ THEORY AND OPTICAL DATA ANALYSIS

The Casimir force $F_{\mathrm{Cas}}(d)$ in Eq. (2) is given by [6]

$$F_{\mathrm{Cas}}(d) = \frac{k_B\, T}{\pi} \sum_{l=0}^{\infty}{}' \sum_{\nu=\mathrm{TE,TM}} \times \int_0^\infty dk\, k\, k_0 \frac{r_\nu^{(1)} r_\nu^{(2)} \exp\left(-2k_0 d\right)}{1 - r_\nu^{(1)} r_\nu^{(2)} \exp\left(-2k_0 d\right)}. \tag{A1}$$

The imaginary frequencies $_{l}$ in Eq. (A1) are defined by the relation $_{l} = (2\pi kT/\hbar)\, l$. The prime in the first summation indicates that the term corresponding to $l = 0$ should be multiplied by a factor of 1/2. The Fresnel reflection coefficients are given by $r_{\mathrm{TE}}^{(i)} = (k_0 - k_i)/(k_0 + k_i)$ and $r_{\mathrm{TM}}^{(i)} = (\varepsilon_{\mathrm{i}}\, k_0 - \varepsilon_0\, k_i)/(\varepsilon_{\mathrm{i}}\, k_0 + \varepsilon_0\, k_i)$ for the transverse electric (TE) and magnetic (TM) field polarizations, respectively. $k_i = \sqrt{\varepsilon_i\,(\mathrm{i}\xi_l)\, \xi^2/c^2 + k_\perp^2}$ (i = 0, 1, 2) represents the out-of plane wave vector in the gap between the interacting plates (k_0), and in each of the interacting plates ($k_{\mathrm{i}=(1,2)}$), as well as $k_\perp$ is the in-plane wave vector.

Furthermore, $\varepsilon(\mathrm{i}\xi)$ is the dielectric function evaluated at imaginary frequencies, which is necessary for calculating the Casimir force between real materials using Lifshitz theory. Applying the Kramers-Kronig relation, $\varepsilon(\mathrm{i}\xi)$ is given by [12]

$$\varepsilon(\mathrm{i}\xi) = 1 + \frac{2}{\pi} \int_0^\infty \frac{\omega\, \varepsilon''(\omega)}{\omega^2 + \xi^2}\, d\omega. \tag{A2}$$

For the calculation of the integral in Eq. (A2) one needs the measured data for the imaginary part of the frequency dependent dielectric function $\varepsilon''(\omega)$. The experimental data for the imaginary part of the dielectric function

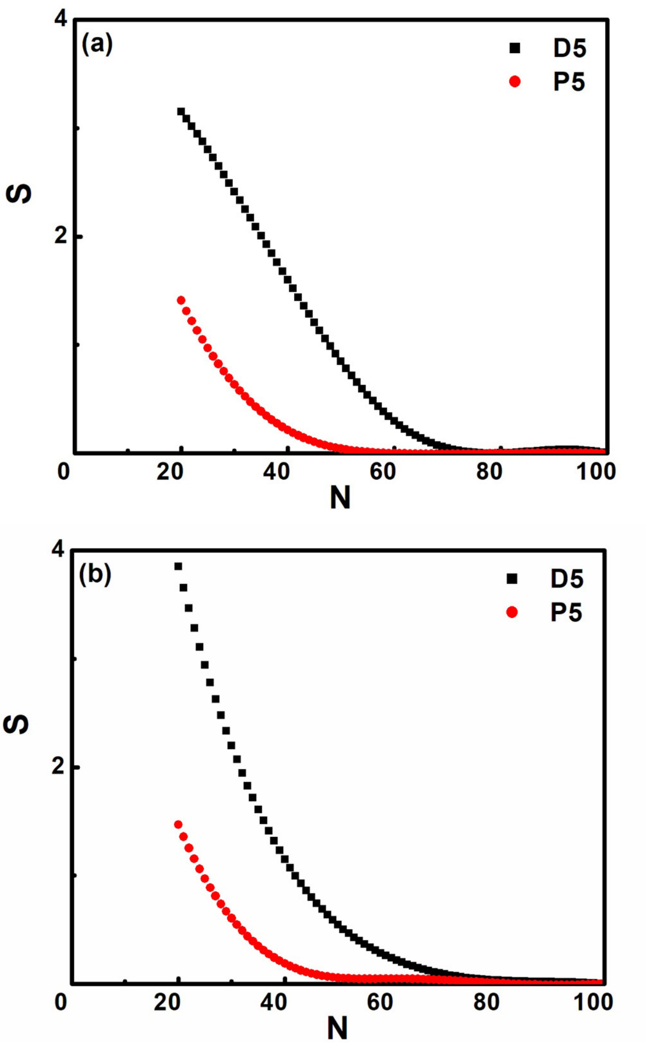

FIG. 15. Area of stable motion S (large diameter × short diameter) vs N (number of oscillation) for sample 5 for both the Drude and plasma models. (a) $p = 0$ (electrostatically unbalanced case), and (b) $p = 1$ (electrostatically balanced case).

cover only a limited range of frequencies ω_1 (=0.03 ev) $< \omega < \omega_2$ (=8.9 ev). Therefore, for the low optical frequencies ($\omega < \omega_1$) we extrapolated using the Drude model [12,36],

$$\varepsilon''_L(\omega) = \frac{\omega_p^2\,\omega_\tau}{\omega\left(\omega^2 + \omega_\tau^2\right)}, \tag{A3}$$

where ω_p is the plasma frequency, and ω_τ is the relaxation frequency. For the high optical frequencies ($\omega > \omega_2$) we extrapolated using the expression [12,32,36]

$$\varepsilon''_H(\omega) = \frac{\mathrm{A}}{\omega^3}. \tag{A4}$$

Using Eqs. (A2)–(A4) $\varepsilon(\mathrm{i}\xi)$ in terms of the Drude model is given by [32,36]

$$\begin{aligned}\varepsilon(\mathrm{i}\xi)_D = 1 + \frac{2}{\pi} + \int_{\omega_1}^{\omega_2} \frac{\omega\,\varepsilon''_{\exp}(\omega)}{\omega^2 + \xi^2}\,d\omega \\ + \Delta_L\varepsilon(\mathrm{i}\xi) + \Delta_H\varepsilon(\mathrm{i}\xi),\end{aligned} \tag{A5}$$

with

$$\begin{aligned}\Delta_L\varepsilon(\mathrm{i}\xi) &= \frac{2}{\pi}\int_0^{\omega_1} \frac{\omega\,\varepsilon''_L(\omega)}{\omega^2 + \xi^2}\,d\omega \\ &= \frac{2\omega_p^2\omega_\tau}{\pi\left(\xi^2 - \omega_\tau^2\right)}\left[\frac{\arctan\left(\frac{\omega_1}{\omega_\tau}\right)}{\omega_\tau} - \frac{\arctan\left(\frac{\omega_1}{\xi}\right)}{\xi}\right],\end{aligned} \tag{A6}$$

and

$$\begin{aligned}\Delta_H\varepsilon(\mathrm{i}\xi) &= \frac{2}{\pi}\int_{\omega_2}^{\infty} \frac{\omega\,\varepsilon''_H(\omega)}{\omega^2 + \xi^2}\,d\omega \\ &= \frac{2\omega_2^3\,\varepsilon''(\omega_2)}{\pi\xi^2}\left[\frac{1}{\omega_2} - \frac{\frac{\pi}{2} - \arctan\left(\frac{\omega_2}{\xi}\right)}{\xi}\right].\end{aligned} \tag{A7}$$

Finally, for the plasma model one must replace the term $\Delta_L\varepsilon(\mathrm{i}\xi)$ in Eq. (A5) with ω_p^2/ξ^2. Therefore, for the plasma model $\varepsilon(\mathrm{i}\xi)$ is given by

$$\varepsilon(\mathrm{i}\xi)_P = 1 + \frac{2}{\pi}\int_{\omega_1}^{\omega_2} \frac{\omega\varepsilon''_{\exp}(\omega)}{\omega^2 + \xi^2}d\omega + \frac{\omega_p^2}{\xi^2} + \Delta_H\varepsilon(\mathrm{i}\xi). \tag{A8}$$

---

[1] A. W. Rodriguez, F. Capasso, and S. G. Johnson, Nat. Photonics **5**, 211 (2011).

[2] F. Capasso, J. N. Munday, and D. Iannuzzi, and H. B. Chan, IEEE J. Sel. Top. Quantum Electron. **13**, 400 (2007).

[3] P. Ball, Nature **447**, 772 (2007).

[4] M. Bordag, G. L. Klimchitskaya, U. Mohideen, and V. M. Mostepanenko, *Advances in the Casimir Effect* (Oxford University Press, New York, 2009).

[5] P. W. Milonni, *The Quantum Vacuum: An Introduction to Quantum Electrodynamics* (Academic, New York, 1993).

[6] H. B. G. Casimir, Proc. K. Ned. Akad. Wet. **51**, 793 (1948).

[7] G. Palasantzas and J. Th. M. DeHosson, Phys. Rev. B. **72**, 121409(R) (2005); **72**, 115426 (2005).

[8] F. Tajik, M. Sedighi, M. Khorrami, A. A. Masoudi, and G. Palasantzas, Phys. Rev. E **96**, 042215 (2017); F. Tajik, M. Sedighi, and G. Palasantzas, J. Appl. Phys. **121**, 174302 (2017).

[9] J. Israelachvili, *Intermolecular and Surface Forces* (Academic, New York, 1992).

[10] R. S. Decca, D. López, E. Fischbach, G. L. Klimchitskaya, D. E. Krause, and V. M. Mostepanenko, Phys. Rev. D **75**, 077101 (2007); Ann. Phys. **318**, 37 (2005); C.-C. Chang, A. A. Banishev, R. Castillo-Garza, G. L. Klimchitskaya, V. M. Mostepanenko, and U. Mohideen, Phys. Rev. B **85**, 165443 (2012); H.-C. Chiu, G. L. Klimchitskaya, V. N. Marachevsky, V. M. Mostepanenko, and U. Mohideen, *ibid.* **81**, 115417 (2010); F. Chen, U. Mohideen, G. L. Klimchitskaya, and V. M. Mostepanenko, Phys. Rev. A **66**, 032113 (2002).

[11] M. Sedighi and G. Palasantzas, J. Appl. Phys. **117**, 144901 (2015).

[12] E. M. Lifshitz, Sov. Phys. JETP **2**, 73 (1956); I. E. Dzyaloshinskii, E. M. Lifshitz, and L. P. Pitaevskii, Sov. Phys.-Usp. **4**, 153 (1961).

[13] F. Intravaiv, S. Koev, I. W. Jung, A. A. Talin, P. S. Davids, R. S. Decca, V. A. Aksvuk, D. A. R. Dalvit, and D. Lopez, Nat. Commun. **4**, 2515 (2013).

[14] Y. Nemirovsky and O. Degani, J. Microelectromech. Syst. **10**, 601 (2001).

[15] O. Degani and Y. Nemirovsky, J. Microelectromech. Syst. **11**, 20 (2002).

[16] J. G. Guo and Y. P. Zhao, Int. J. Solids Struct. **43**, 675 (2006).

[17] R. Satter, F. Plötz, G. Fattinger, and G.Wachutka, Sens. Actuators, A **97–98**, 337 (2002).

[18] O. Bochobza-Degani and Y. Nemirovsky, Sens. Actuators, A **97–98**, 569 (2002).

[19] V. B. Svetovoy, P. J. van Zwol, G. Palasantzas, and J. T. M. De Hosson, Phys. Rev. B **77**, 035439 (2008).

[20] F. Tajik, M. Sedighi, A. A. Masoudi, H. Waalkens, and G. Palasantzas, Phys. Rev. E **98**, 022210 (2018).

[21] R. L. Olmon, B. Slobick, T. W. Johnson, D. Shelton, S.-H. Oh, G. D. Boreman, and M. B. Raschke, Phys. Rev. B **86**, 235147 (2012).

[22] J. A. Woollam Co. Inc., http://www.jawoollam.com.

[23] M. Taghizadeh and H. Mobki, Arch. Mech. **66**, 95 (2014).

[24] W. H. Lin and Y. P. Zhao, J. Phys. D: Appl. Phys. **40**, 1649 (2007).

[25] G. Torricelli, P. J. van Zwol, O. Shpak, C. Binns, G. Palasantzas, B. J. Kooi, V. B. Svetovoy, and M. Wuttig, Phys. Rev. A **82**, 010101(R) (2010).

[26] O. Degani, E. Socher, A. Lipson, T. Lejtner, D. J. Setter, Sh. Kaldor, and Y. Nemirovsky, J. Microelectromech. Syst. **7**, 373 (1998).

[27] R. García and R. Perez, Surf. Sci. Rep. **47**, 197 (2002); M. Li, H. X. Tang, and M. L. Roukes, Nat. Nanotechnol **2**, 114 (2007).

[28] S. K. Lamoreaux, Phys. Rev. Lett. **78**, 5 (1997); Rep. Prog. Phys. **68**, 201 (2005); H. B. Chan, V. A. Aksyuk, R. N. Kleiman, D. J. Bishop, and F. Capasso, Phys. Rev. Lett. **87**, 211801 (2001); Science **291**, 1941 (2001); R. Guerout, J. Lussange, H. B. Chan, A. Lambrecht, and S. Reynaud, Phys. Rev. A **87**, 052514 (2013); J. Zou, Z. Marcet, A. W. Rodriguez, M. T. H. Reid, A. P. McCauley, I. I. I. Kravchenko, T. Lu, Y. Bao, S. G. Johnson, and H. B. Chan, Nat. Commun. **4**, 1845 (2013); L. Tang, M. Wang, C. Y. Ng, M. Nikolic, C. T. Chan, A. W. Rodriguez, and H. B. Chan, Nat. Photonics **11**, 97 (2017); A. W. Rodriguez, P.-C. Hui, D. P. Woolf, S. G. Johnson, M. Loncar, and F. Capasso, Ann. Phys. (Berlin) **527**, 45 (2015).

[29] M. Sedighi, W. H. Broer, G. Palasantzas, and B. J. Kooi, Phys. Rev. B **88**, 165423 (2013).

[30] S. Cui and Y. C. Soh, J. Microelectromech. Syst. **19**, 1153 (2010).

[31] T. G. Philbin and U. Leonhardt, Phys. Rev. A **78**, 042107 (2008).

[32] M. Sedighi, V. B. Svetovoy, and G. Palasantzas, Phys. Rev. B **93**, 085434 (2016).

[33] M. W. Hirsch, S. Smale, and R. L. Devaney, *Differential Equations, Dynamical Systems, and an Introduction to Chaos* (Elsevier Academic Press, San Diego, CA, 2004).

[34] W. Broer, H. Waalkens, V. B. Svetovoy, J. Knoester, and G. Palasantzas, Phys. Rev. Appl. **4**, 054016 (2015).

[35] M. Siewe and U. H. Hegazy, Appl. Math. Modell. **35**, 5533 (2011).

[36] M. Sedighi, V. B. Svetovoy, W. H. Broer, and G. Palasantzas, Phys. Rev. B **89**, 195440 (2014).